A mathematical model for describing the retinal nerve fiber bundle trajectories in the human eye

Jansonius, Nomdo M.; Schiefer, Julia; Nevalainen, Jukka; Paetzold, Jens; Schiefer, Ulrich

A mathematical model for describing the retinal nerve fiber bundle trajectories in the human eye: average course, variability, and influence of refraction, optic disc size and optic disc position

Nomdo M. Jansonius,[1,2*] Julia Schiefer,[3*] Jukka Nevalainen,[4] Jens Paetzold,[5] Ulrich Schiefer[5]

1. Department of Ophthalmology, University of Groningen, University Medical Center Groningen, Groningen, The Netherlands
2. Department of Epidemiology, Erasmus Medical Center, Rotterdam, The Netherlands
3. University Eye Hospital Munich, Ludwig Maximilians University, Munich, Germany
4. University Eye Hospital Oulu, Oulu, Finland
5. Centre for Ophthalmology, University of Tübingen, Tübingen, Germany

* Contributed equally to this article

Correspondence: Prof. N.M. Jansonius, Department of Ophthalmology, University Medical Center Groningen, University of Groningen, P.O.Box 30.001, 9700 RB Groningen, The Netherlands. Tel: +31 50 3612510; Fax: +31 50 3611709; Email: n.m.jansonius@umcg.nl

Abstract

Previously we developed a mathematical model for describing the retinal nerve fiber bundle trajectories in the superior-temporal and inferior-temporal regions of the human retina, based on traced trajectories extracted from fundus photographs. Aims of the current study were to (i) validate the existing model, (ii) expand the model to the entire retina and (iii) determine the influence of refraction, optic disc size and optic disc position on the trajectories. A new set of fundus photographs was collected comprising 28 eyes of 28 subjects. From these 28 photographs, 625 trajectories were extracted. Trajectories in the temporal region of the retina were compared to the existing model. In this region, 347 of 399 trajectories (87%) were within the 95% central range of the existing model. The model was extended to the nasal region. With this extension, the model can now be applied to the entire retina that corresponds to the visual field as tested with standard automated perimetry (up to approximately 30 deg eccentricity). There was an asymmetry between the superior and inferior hemifields and a considerable location-specific inter-subject variability. In the nasal region, we found two "singularities", located roughly at the one and five o'clock positions for the right optic disc. Here, trajectories from relatively widespread areas of the retina converge. Associations between individual deviations from the model and refraction, optic disc size and optic disc position were studied with multiple linear regression. Refraction ($P=0.021$) and possibly optic disc inclination ($P=0.09$) influenced the trajectories in the superior-temporal region.

1. Introduction

In contrast to lesions of the outer retinal layers, which are characterized by a clear structure-function relationship, retinal nerve fiber layer (RNFL) loss shows a characteristic disparity between lesion site and resulting functional loss (Trobe, 2001). This disparity is structurally related to the characteristic axonal pathway of the retinal ganglion cells (Hoyt et al., 1973; Minckler, 1980; Garvin et al., 2012).

Examination and evaluation of the RNFL is an important clinical diagnostic tool in any kind of optic neuropathy, including glaucoma. RNFL photography is a sensitive method for the detection of retinal nerve fiber bundle (RNFB) loss (Iwata et al., 1982; Airaksinen et al., 1983; Sommer et al., 1983; Airaksinen et al., 1985; Quigley et al., 1994; Tuulonen et al., 2000). This important technique has been replaced largely by automated morphometric methods for analyzing and quantifying the optic nerve head (Heidelberg Retina Tomograph [HRT]; Heidelberg Engineering GmbH, Heidelberg, Germany; Rohrschneider et al., 1994), the peripapillary RNFL (laser polarimetry [GDx]; Carl Zeiss Meditec Inc., Dublin, CA, USA; Weinreb et al., 1990; Dreher, 1992) or both (optical coherence tomography [OCT]; Hee et al., 1995). With the introduction of these new techniques, an important aspect of glaucoma assessment has been lost: taking into account the characteristic course of the RNFBs along the retinal surface (Lee et al., 2012).

A detailed knowledge of the RNFB trajectories is a prerequisite for incorporating it in glaucoma assessment, for example in new perimetric techniques like fundus oriented perimetry (Schiefer et

al., 2003) and scotoma oriented perimetry (Paetzold et al., 2005) and in the use of existing techniques (Nouri-Mahdavi et al., 2012). Although it may be possible to measure these trajectories in individual patients in the near future (Garvin et al., 2012), it might be sufficient for certain purposes to assume a general trajectory pattern. Moreover, algorithms for detecting trajectories in individual patients can be made more accurate and efficient by incorporating a general trajectory pattern as prior knowledge.

Several descriptions of the RNFB trajectories have been made in the past (Vrabec, 1966; Fitzgibbon and Taylor, 1996; Weber and Ulrich, 1991; Garway-Heath et al., 2000; Wigelius, 2001; Ferreras et al., 2008; Turpin et al., 2009). Similar to Weber and Ulrich, Garway-Heath et al. created a map, showing a limited number of visual field sectors connected to large optic disc sectors. Although the sizes of these sectors are in line with inter-subject variability, the approach could erroneously be misinterpreted because of the sharp borders between the sectors.

Jansonius et al. (2009) introduced a mathematical model describing the RNFB trajectories and their inter-subject variability, based on traced trajectories extracted from fundus photographs. At present this model does not consider the nasal retina. Furthermore, sources of variability were not addressed in that study. Factors that may influence the individual trajectory pattern are refraction/axial length, optic disc size and optic disc position (Denniss et al., 2012; Lamparter et al., 2012).

The aims of the present study were (i) to validate the previous model in an independent dataset, (ii) to expand the model to the

entire retina and (iii) to determine the influence of refraction, optic disc size and optic disc position on the trajectories.

2. Material and methods

2.1. Patient data and data acquisition

We collected retrospectively 56 fundus images of 28 patients who underwent digitized fundus photography as part of regular care in the University Eye Hospital Oulu, Finland. For this study, only the right eye of each subject was included. Only subjects without diseases affecting the RNFL or its visibility were included in this study. As a consequence, most patients were relatively young (mean age 28 years) diabetic patients without diabetic retinopathy. Selection was performed with regard to the spherical equivalent refraction (SE) in order to get sufficient variability for studying the influence of SE on the retinal nerve fiber bundle trajectories. Approval for the study was obtained according to the guidelines of the Ethical Committee of the Northern Ostrobothnia Hospital District. All subjects provided written informed consent for the anonymous analysis of their fundus pictures and check of their patient file for refraction data and ophthalmic and neurological history. The study followed the tenets of the declaration of Helsinki.

Photographs were taken in mydriasis with two different fundus cameras (Canon CF-60 UVi (18 subjects) or Canon CF-60 DSi (10 subjects); Canon Inc., Utsunomiya, Japan) with a built-in blue interference filter of 495 nm wavelength at an angle of 60 deg

(Airaksinen et al., 1982). Resolutions were 3504 by 2336 pixels (CF-60 UVi) and 5616 by 3774 pixels (CF-60 DSi). One of the authors (JS) traced 24 trajectories per fundus photograph, one per half clock-hour. It was not possible to trace all 24 trajectories in all photographs (see Results section). For inclusion, at least 12 trajectories had to be traceable with no more than one per half clock-hour and at least one in every quadrant; trajectories had to start within 5° from the center of the optic disc and had to have a minimum length depending on the clock hour (Table 1 in Jansonius et al., 2009). Figure 1 shows an example of a traced photograph. A subset of trajectories was also traced by another author (JN) and this subset was used to evaluate inter-observer variability. To avoid a selection bias here, a masked author (NJ) selected - from the originally traced trajectories - at random 24 of 28 fundus images and subsequently at random one trajectory per fundus image in such a way that there was one trajectory per half clock-hour. This selection was based on fundus IDs and trajectory IDs only; the images were not available at the time of the selection. The selected trajectories were marked and formed the inter-observer variability subset.

2.2. Factors possibly associated with trajectories

Here, we studied refraction, optic disc size and optic disc position. For studying the influence of refraction, the subjects were stratified according to SE in three groups: myopia (SE ≤ -1.00 D), emmetropia, and hyperopia (SE ≥ +1.00 D). The SE was also treated as a continuous variable. Optic disc area was calculated from the digital RNFL photographs using an algorithm introduced by Bartling et al. (2008). As a measure of optic disc position, we

determined the inclination of the optic disc, that is, the angle between a line through the centers of the fovea and optic disc and a horizontal line through the center of the fovea.

2.3. Data analysis

The position of the fovea and the center of the optic disc were marked on each image. The images were superimposed by translation in order to center the fovea, followed by rotation and zooming to align the centers of the optic discs, as described earlier (Jansonius et al 2009). The trajectories were stored in a modified polar coordinate system (r, φ), with its center located in the center of the optic disc at an eccentricity of 15°, 2° above the horizontal meridian. Here, r represents the distance from the center of the disc and φ the corresponding angle, as illustrated in Figure 2. The transformation from a Cartesian coordinate system with its center at the fovea *(*x,y) to this polar coordinate system and the corresponding inverse transformation have been described earlier (Jansonius et al., 2009).

The trajectories were fitted in the modified polar coordinate system. In this coordinate system, the trajectories were described by (Jansonius et al., 2009):

$$\phi(\phi_0, r) = \phi_0 + b(\phi_0) \cdot (r - r_0)^{c(\phi_0)}$$

(1)

where $\varphi_0 = \varphi(r=r_0)$ is the angular position of the trajectory at its starting point at a circle with radius r_0 around the center of the

disc, *b* a real number and *c* a positive real number. As it was not possible to follow the trajectories closer than typically 3-5° to the center of the disc, r_0 was set to 4°.

The required nonlinear fitting was solved by performing a two-stage fitting process. In the first stage, the relationship between *c* and φ_0 was evaluated and substituted in Eq. (1). Here, we used the previously evaluated relationship, being:

$$c = 1.9 + 1.4 \tanh\{(\varphi_0-121)/14\}$$

$$(2)$$

for the superior hemifield and:

$$c = 1.0 + 0.5 \tanh\{(-\varphi_0-90)/25\}$$

$$(3)$$

for the inferior hemifield. Figure 2 illustrates the influence of *c* on the trajectories. Parameter *c* determines the location of the curvature (punctum maximum of curvature close to the disc for *c* < 1 and further away from the disc for *c* > 1) while *b* determines the amount of curvature. After substituting Eqs. (2) and (3) in Eq. (1), Eq. (1) was transformed into:

$$y = b(\varphi_0) \ x$$

$$(4)$$

where *y* is $\varphi-\varphi_0$ and *x* is $(r-r_0)^c$. In the second stage of the fitting process, Eq. (4) was fitted using least-squares fitting, and this

fitting was repeated for a range of φ_0 values around the estimated value in 0.1 deg steps. The fit with the lowest root mean square (RMS) value was considered the final fit. The fitting was performed using Fortran 77 (FORTRAN Optimizing Compiler Version 4.10; Microsoft, Redmond, WA, USA) and yielded for all trajectories a φ_0, b and RMS value. The RMS value was defined as:

$$RMS = \sqrt{\frac{1}{n} \sum_{i=1}^{n} (\phi_i - \hat{\phi}_i)^2}$$

(5)

where n is the number of sampled data points in the trajectory, φ_i the measured value of φ for the i-th datapoint and $\hat{\phi}_i$ the corresponding fitted value.

Our original model was limited to the superior-temporal ($60 \leq \varphi_0 \leq 180°$) and inferior-temporal ($-180 < \varphi_0 \leq -60°$) regions. Within these regions, the b values of the newly traced trajectories were compared to the previously found relationship between φ_0 and b. This relationship is:

$$\ln b = -1.9 + 3.9 \tanh\{-(\varphi_0-121)/14\}$$

(6)

for the superior-temporal region and:

$$\ln(-b) = 0.7 + 1.5 \tanh\{-(-\varphi_0-90)/25\}$$

(7)

for the inferior-temporal region. We determined the average

difference between the ln b (superior-temporal) and ln($-b$)

(inferior-temporal) values of the newly traced trajectories and the

existing model (bias) and the corresponding variability. Results

were presented as mean difference with standard deviation or as

median difference with inter-quartile range (IQR), depending on the

distribution of the residuals. Normality was checked using a

Shapiro-Francia W' test. We also determined the percentage of the

newly traced trajectories that had a (φ_0,b) combination within the

95% central range of the existing model (Jansonius et al., 2009).

These percentages were also determined after stratification for SE;

differences between myopia, emmetropia and hyperopia were analyzed

with a chi-squared test.

The influence of factors possibly associated with the trajectories

(refraction, optic disc size and optic disc position) was further

studied by plotting individual deviations from the model against the

various factors and by performing multiple linear regression

analysis. This was done for the superior-temporal and inferior-

temporal regions separately. Outcome measure was the "mean

departure". The mean departure of a subject was, for the superior-

temporal region, defined as the difference between ln b and the

model, averaged over all traced trajectories with $60 \leq \varphi_0 \leq 180°$; for

the inferior-temporal region, the mean departure of a subject was

defined as the difference between ln($-b$) and the model, averaged

over all traced trajectories with $-165 < \varphi_0 \leq -60°$ (inferior

papillomacular bundle excluded from this analysis [see Results and

Discussion sections]). A Pearson's correlation matrix was made to

uncover multicollinearity. In the case of correlation coefficients

exceeding 0.8, only one of the factors involved was entered in the

multiple linear regression analysis. Factors with P<0.2 in the initial multiple linear regression analysis were transferred to the final model.

Inter-observer variability of the trajectory-tracing process was analyzed by calculating the median difference (bias) and corresponding IQR for ln b (superior-temporal) and ln($-b$) (inferior-temporal) for the subset of trajectories traced by two observers. We also made a paired comparison with a Wilcoxon test.

For the nasal region ($-60 < \varphi_0 < 60°$), we plotted the traced trajectories as datapoints in a φ_0-b plane and fitted the data by a second-degree polynomial, yielding the relationship between b and φ_0. For determining the corresponding 95% central range, the nasal region was divided in 20° segments and we calculated the mean b value and corresponding standard deviation for each segment. Subsequently, we determined the 95% central range by fitting second-degree polynomials to the resulting b minus two standard deviations (lower limit) and b plus two standard deviations (upper limit) values. The existing model and the newly described nasal region were combined into a final model for the description of the retinal nerve fiber bundle trajectories for the entire human retina.

An inverse of the final model was evaluated numerically. For each test location of the 30-2 6x6° grid of the Humphrey field analyzer (Carl Zeiss Meditec Inc., Dublin, California, USA), the average value and the 95% central range of φ_0 were determined. For the inverse model, Mathematica 4.0.1.0 (Wolfram Research Inc., Champaign, IL, USA) was used.

A P-value of 0.05 or less was considered statistically significant.

3. Results

Of the included 28 eyes of 28 subjects, 9 were classified as myopic (median SE -4.00 D; range -8.75 to -1.25 D), 10 as emmetropic (median SE 0.00 D; range -0.75 to +0.50 D) and 9 as hyperopic (median SE +1.50 D; range +1.00 to +6.25 D). On average 22.3 of the aimed 24 trajectories per fundus were traceable. The major reason for not being able to trace at least one trajectory in a certain half clock-hour was insufficient visibility of the trajectories, which occurred mainly on the nasal side of the optic disc. Of the resulting 625 traced trajectories, 195 were from eyes with myopia, 222 from eyes with emmetropia and 208 from eyes with hyperopia. Figure 3 shows the raw traced trajectories, stratified for SE. The proximal end of the trajectories was always between 4° (r_0 in the model; 79% of the trajectories could be traced up to 4°) and 5° (the maximum allowed distance). The median (IQR; range) length was 16° (13 to 22°; 10 to 38°).

Table 1A shows the RMS values of the traced trajectories fitted by Eq. (1); Table 1B gives the corresponding RMS values of the traced trajectories fitted by Eq. (4). The former depicts the accuracy of the underlying basic assumption as given in Eq. (1); the latter the accuracy of the overall fit. As can be seen in this Table, the accuracy of either the underlying basic assumption or of the overall fit did not depend on refraction.

Figure 4 presents parameter b (amount of curvature; defined in Eq. (1)) resulting from the second stage of the fitting process as a function of φ_0 for the superior (**A**) and inferior (**B**) hemifields. As can be seen in this figure, there appeared to be two "singularities", at approximately $\varphi_0 = +60°$ and $\varphi_0 = -60°$. At these singularities, a wide range of b values occur at the same φ_0 value – a phenomenon that can be seen in the raw data as well (Figure 3; black dots).

Figure 5 shows the same parameter b as a function of φ_0, now presented as ln b for the superior-temporal region (**A**) and ln($-b$) for the inferior-temporal region (**B**). The lines represent the average fits with corresponding 95% central ranges from the earlier published model (Jansonius et al., 2009). In these regions (comprising 399 [227 superior-temporal and 172 inferior-temporal] of the 625 traced trajectories), 347 of 399 trajectories (87%) were within the 95% central range of the model. After stratification for SE, this was the case in 104 of 118 (88%) for myopia, 129 of 149 (87%) for emmetropia and 114 of 132 (86%) for hyperopia (P=0.91). A significant deviation from the model occurred only in the inferior papillomacular bundle (see Discussion). This deviation appeared not to be related to the SE. After the exclusion of trajectories with φ_0 < -165°, 342 of 379 trajectories (90%) were within the 95% central range of the model. The median difference (IQR) between ln b and the model for the 227 trajectories in the superior-temporal region was 0.04 (0.47 [-0.22 to 0.25]); the median difference (IQR) between ln($-b$) and the model for the 172 trajectories in the inferior-temporal region was 0.06 (0.57 [-0.26 to 0.31]).

The inter-observer variability analysis showed a median difference (IQR) of ln b of 0.02 (0.25) for the superior-temporal region and a median difference (IQR) of ln($-b$) of 0.00 (0.16) for the inferior-temporal region. Differences between the observers were not significant (P=0.89 and P=0.58 for the superior-temporal and inferior-temporal region, respectively).

Figure 6 shows parameter b resulting from the second stage of the fitting process as a function of φ_0 for the nasal region. The lines represent the average fit with corresponding 95% central range, mathematically described by, respectively:

$$b = 0.00083 \ \varphi_0^2 + 0.020 \ \varphi_0 - 2.65$$

$$(8)$$

$$b = 0.00050 \ \varphi_0^2 - 0.011 \ \varphi_0 - 6.80$$

$$(9)$$

and

$$b = 0.00120 \ \varphi_0^2 + 0.050 \ \varphi_0 + 1.51$$

$$(10)$$

For this fit, the outliers at $\varphi_0 = -60°$ and $\varphi_0 = +60°$ were excluded (see Discussion).

Figure 7A presents the final model for the nerve fiber trajectories, in 10-degree steps. Figure 7B shows the inverse representation, with test locations from the 30-2 6x6° grid of the Humphrey Field Analyzer connected to the corresponding parts of the optic nerve

head circumference (presented as mean φ_0 values with corresponding 95% central ranges). Depending on the location of the visual field test location, the standard deviation of this angular location at the optic nerve head circumference (calculated as one quarter of the 95% central range) ranged for the superior hemifield from less than 1 to 11.0°, with a median value of 7.5°, and for the inferior hemifield from less than 1 to 14.8°, with a median value of 9.0°.

Figure 8 shows the influence of refraction, optic disc size and optic disc position on the trajectories, for the superior-temporal (left column) and inferior-temporal (right column) regions. At first glance, none of these factors seemed to have a significant influence on the trajectories. The correlation matrix showed a correlation coefficient of 0.243 for SE versus optic disc size, 0.143 for SE versus optic disc inclination and -0.192 for optic disc size versus optic disc inclination. Refraction, optic disc size and optic disc inclination were entered in the multiple linear regression analyses. Table 2 presents the results for outcome measure mean departure. The explained variances (R^2) were 0.28 and 0.08 for the superior-temporal (Table 2A) and inferior-temporal (Table 2B) region, respectively. Refraction was the only significant independent variable in the final model for the superior-temporal region (P=0.021) with apparently some influence of optic disc inclination as well (P=0.09). In the inferior-temporal region, none of the factors appeared to influence the trajectories significantly. The correlation coefficient of the mean departure superior-temporal versus the mean departure inferior-temporal was 0.21 (95% confidence interval -0.18 to 0.55).

4. Discussion

The previously published mathematical model for the RNFL trajectories in the superior-temporal and inferior-temporal regions of the retina was validated and the model was extended to the entire circumference of the optic nerve head, yielding a complete description of the wiring of the human retina up to an eccentricity of approximately 30°. We found an asymmetry between the superior and inferior hemifields and a considerable location-specific inter-subject variability. Some of this variability was explained by refraction and possibly optic disc inclination.

4.1. Comparison with previous model

A significant deviation from the model occurred only in the inferior papillomacular bundle ($\varphi_0 < -165°$). This deviation was not observed in the previous study as there were essentially no trajectories traced in that region. Although the deviation seems large, it should be noted that $-b$ is very close to zero in that region; the interpretation of the deviation is that the (purple-red) trajectory labeled -170 in Fig. 7A should have a slightly more straight course.

4.2. Extension of the model – singularities

The model was extended to the nasal retina. Here, we found two singularities, at approximately $\varphi_0 = +60°$ and $\varphi_0 = -60°$. It is important to realize that neither the modified polar coordinate system, nor the basic assumption on the trajectories (Eq. [1]), nor the relationship between c and φ_0 (Eqs. [2] and [3]) has any discontinuity at either $\varphi_0 = +60°$ or $\varphi_0 = -60°$. Hence, the

singularities as observed in Figs. 4A and 4B cannot be an artifact

of the applied methodology. At the superior singularity ($\varphi_0 = +60°$),

trajectories from a wide range of directions converge, depicted by a

wide range of b values occurring at the same φ_0 value of

approximately +60°. At the inferior singularity ($\varphi_0 = -60°$), a

similar phenomenon can be observed but with a different pattern.

Here, unlike at the superior singularity, the b values display a

clear discontinuity. The apparent interpretation of this

discontinuity is a "gap", that is, a wedge-shaped sector of the

retina not connected to the optic disc. This gap can be observed in

both the raw data (Fig. 3) and the final model (Fig. 7A). Obviously,

such a gap does not exist, except for a pathological entity known as

retinal colobomata (Mann, 1957; Onwochei et al., 2000). A closer

look to our photographs revealed without doubt trajectories in the

gap, but their visibility did not start within 5° from the center of

the optic disc (one of our inclusion criteria) and for that reason

they were originally not included. To further explore this, we

traced yet an additional two to four trajectories in the gap for all

included photographs – now ignoring the requirement that the

trajectories had to start within 5° from the center of the optic

disc. Figure 9A shows the original trajectories as displayed in Fig.

3 colored gray and the additionally traced trajectories colored red.

Figure 9B presents the original datapoints as displayed in Fig. 4B

with the b values of the additionally traced trajectories added.

Interestingly, the addition of the datapoints in Fig. 9B did not

result in a continuous pattern as found in the superior singularity

(Fig. 4A) but rather accentuated the discontinuity (turquoise-

colored areas in Fig. 9B). Hence, although a singularity was found

in both hemifields, these two singularities seem to differ in

nature. Superiorly, the singularity seems to be a region where

trajectories from a relatively large area of the retina converge apparently at random; inferiorly, this convergence seems to be organized to some extent in the z direction (that is, perpendicular to the retina). A tentative speculation could be that this asymmetry is related to the closure of the fetal fissure. From the point of view of glaucoma diagnostics both singularities behave identically: at both singularities the spatial relationship between structure and function is poorly defined.

4.3. Retinal nerve fiber layer is a three-dimensional structure

Conventional fundus photography reduces the three-dimensional retinal structure into a two-dimensional image; information in the z direction is – with a few exceptions - not available. One of the exceptions is the inferior singularity as discussed in the previous paragraph. Our detailed analysis of the singularity revealed that trajectories from different layers may cross rather than that they follow the same course in all layers. Crossing trajectories have been reported before by Jeoung et al. (2008). In general, however, only the uppermost trajectories – facing the inner limiting membrane - are visible. Only in the case of manifest RNFL damage, deeper layers become visible and they have been studied before. Radius and Anderson (1979) and Minckler (1980) have demonstrated that fibers originating in the peripheral retina are situated deep in the RNFL and are located in the periphery of the optic nerve, close to the edge of the scleral canal. According to Garway-Heath et al. (2000), the retinal nerve fibers do not seem to be highly organized within the deeper retinal layers – with exception of fibers heading towards the temporal raphe and arcuate bundles. All this suggests that our

model will be primarily reliable in the regions of the retina corresponding to the central visual field.

4.4. Bias and variability

Possible factors that could bias the trajectories or cause variability are (1) the fundus photography, (2) patient selection, (3) the tracing process and (4) anatomical differences between subjects. In our earlier study, we used randomly collected fundus photographs obtained from anonymous databases of several participating sites. As a consequence, there was a lack of standardization. In the current study, the fundus images were collected at a single site and processed in a standardized manner. The new data were well described by the earlier model and the variability was similar. This suggests that fundus photography is not a major source of either bias or variability. As mentioned in the Methods section, patient selection was performed intentionally to ensure sufficient variability in SE. Furthermore, most patients were relatively young (because of a better visibility of the RNFL) diabetic patients (the most common indication for fundus photography in clinical practice) without diabetic retinopathy. Here, the assumption was that diabetes does not affect the trajectories or their visibility as long as there is no retinopathy. In the current study, a subset of trajectories was traced by two different observers. There was no bias between the two observers and the inter-observer variability was two to four times smaller than the overall variability. Also, in the earlier study (Jansonius et al., 2009) the tracing process was performed by yet another observer. All this indicates that the tracing process is also not a major source of either bias or variability.

Anatomical differences between subjects are the fourth possible factor that could bias the trajectories or cause variability. Lamparter et al. (2012) studied the influence of axial length, refraction, optic disc size and optic disc position on the model of Garway-Heath et al. (2000). All these factors were shown to influence that model significantly. Denniss et al. (2012) described, in a theoretical nerve growth model, the importance of the vertical optic disc position. Tanabe et al. (2012) measured the RNFL bundle angles using scanning laser ophthalmoscopy and found significant influences of refraction and the architecture of the retinal arteries. We studied the role of refraction, optic disc size and – because our methodology only allowed for the relative position of the optic disc – optic disc inclination. In agreement with Lamparter et al., Denniss et al. and Tanabe et al., we found a significant influence of refraction - but only superiorly (none of the other studies addressed the hemifields separately). Optic disc inclination appeared to have a nonsignificant influence superiorly in our study whereas optic disc size did not have any influence on the trajectories. A possible explanation for the difference in influence of optic disc size between Lamparter et al. and our study is that we used a circle around the optic disc with a radius of 4° whereas Lamparter et al. studied the entry point at the disc margin itself. The overall explained variance (R^2) in our study was 0.28 for the superior-temporal region and even less inferiorly. Interestingly, it was the inferior-temporal region where Jeoung et al. (2008) found the overlapping trajectories – indicating a less strict arrangement of the RNFL in this region. Obviously, other sources of variability remain to be discovered. One possible source could be the

architecture of the retinal arteries (Henkind, 1967; Tanabe et al., 2012).

We preprocessed the images by aligning the fovea and optic disc centers and assuming an optic disc position at an eccentricity of 15°, 2° above the horizontal meridian (2.3). The apparent influence of the optic disc inclination parameter on the mean departure of the model (Table 2) might either indicate real anatomical variability related to the optic disc inclination or indicate an artifact introduced by the alignment process. The results as presented in Table 2 can be used to adjust for this influence on the mean departure. A more-than-average influence of the alignment process on the inter-subject variability could be expected in the papillomacular area. This is not clear in the superior hemifield (Fig. 5A) but the deviation from the model as observed inferiorly (Fig. 5B; 4.1) seems to go together with an increased variability, which could (partially) be related to the alignment process.

4.5. Comparison with literature – asymmetry between hemifields

Many descriptions of the RNFL trajectories have been published before. These descriptions were based on histology in monkey (Vrabec, 1966) or postmortem human eyes (Fitzgibbon and Taylor, 1996), fundus photography (Garway-Heath et al., 2000), ganglion cell densities (Wigelius, 2001), perimetry (Weber and Ulrich., 1991), on correlations between perimetric sensitivities and optic disc anatomy (Ferreras et al., 2008; Turpin et al., 2009) or on optical coherence tomography (Garvin et al., 2012). The agreement between these descriptions and our model has been discussed previously (Jansonius et al., 2009). Compared to the earlier descriptions, our model has

three important features. First, it gives a complete mathematical description of the RNFL trajectories. A mathematical description allows for an easy and flexible incorporating in software. Second, our model describes a clear asymmetry between the superior and inferior hemifields. Asymmetry has been found in some but not all earlier descriptions (Ferreras et al., 2008). One of the consequences of the asymmetry as found in our model is that more clock hours of the superior half of the optic disc than of the inferior half are devoted to the fovea – especially if we also take into account the observed deviation from the model in the inferior papillomacular bundle ($\varphi_0 < -165°$). This might be related to the clinical observation that loss of visual acuity in early glaucoma seems to occur more often in patients with inferior paracentral defects compared to superior paracentral defects. Third, our model provides a detailed location-specific estimate of the magnitude of the variability - resulting in the uncovering of singularities.

4.6. Conclusions

A mathematical model is presented which describes the retinal nerve fiber bundle trajectories for the entire retina up to an eccentricity of approximately 30°, that is, the area corresponding to the visual field as tested with standard automated perimetry. The trajectories display differences between the superior and inferior hemifields. Two singularities exist where the spatial relationship between structure and function is poorly defined. The trajectories show a considerable location-specific inter-subject variability. Refraction and possibly optic disc inclination explain some of this variability in the superior-temporal region but not in the inferior-temporal region. This suggests that, depending on the accuracy

required, the average model may be used or the trajectories have to be determined individually.

Figure captions

Figure 1. Example of a fundus photograph with traced trajectories.

Figure 2. The modified polar coordinate system (for details see Jansonius et al., 2009). Two examples of trajectories illustrate the influence of c on the trajectories.

Figure 3. Superimposition of all 625 included trajectories, stratified for refraction (myopia = blue, emmetropia = green, hyperopia = red). Black dots indicate the approximate location of the two singularities (see text).

Figure 4. Parameter b resulting from the second stage of the fitting process as a function of φ_0 for the superior (**A**) and inferior (**B**) hemifields. Datapoints represent individual trajectories after stratification for refraction in myopia (Δ), emmetropia (O) and hyperopia (+).

Figure 5. Parameter b resulting from the second stage of the fitting process as a function of φ_0, presented as ln b for the superior-temporal region (**A**) and ln($-b$) for the inferior-temporal region (**B**). Datapoints represent individual trajectories after stratification for refraction in myopia (Δ), emmetropia (O) and hyperopia (+); lines represent the average fits with corresponding 95% central ranges from the earlier published model (Jansonius et al., 2009).

Figure 6. Parameter b resulting from the second stage of the fitting process as a function of φ_0 for the nasal region. Lines represent the average fit with corresponding 95% central range. Datapoints

represent individual trajectories after stratification for refraction in myopia (Δ), emmetropia (O) and hyperopia (+).

Figure 7. Final model, average trajectories in 10-degree steps (**A**) and inverse representation, with test locations from the 30-2 6x6° grid of the Humphrey Field Analyzer connected to the corresponding parts of the optic nerve head (**B**). The optic nerve head is presented upright; the visual field grid as projected on the retina, that is, mirrored along the *x*-axis. Numbers represent mean φ_0 values with corresponding 95% central ranges.

Figure 8. Influence of refraction, optic disc size and optic disc inclination on the trajectories, for the superior-temporal (left column) and inferior-temporal (right column) regions. Mean departure along the *y* axes is the average deviation per subject from the model in the concerning region.

Figure 9. Additionally traced trajectories in the inferior-nasal part of the retina (**A**; original trajectories colored gray, additionally traced trajectories red). Parameter *b* resulting from the second stage of the fitting process as a function of φ_0 (**B**; the majority of the additionally traced trajectories lay in the turquoise-colored squares).

Tables

Table 1. Root mean square values (median with interquartile range; deg) corresponding to the first (A) and second (B) stage of the two-stage fitting process, for all included trajectories together and after stratification for refraction

	n	median	inter-quartile range
A			
all	625	0.46	0.20 – 0.95
myopia	195	0.44	0.20 - 0.87
emmetropia	222	0.51	0.20 – 0.95
hyperopia	208	0.47	0.21 – 1.03
B			
all	625	0.71	0.32 – 1.59
myopia	195	0.67	0.30 – 1.50
emmetropia	222	0.77	0.33 – 1.57
hyperopia	208	0.70	0.30 – 1.65

Table 2. Multiple linear regression analyses with the mean departure (average individual deviation from the model) as dependent variable and refraction, optic disc size and optic disc inclination as independent variables for the superior-temporal (A,B) and inferior-temporal (C) regions

	Coefficient	Standard error	P-value
A: superior-temporal			
Intercept	-0.0848		
Refraction (D)	0.0254	0.0121	0.047
Optic disc size (mm^2)	0.0962	0.1016	0.35
Optic disc inclination (°)	-0.0247	0.0164	0.15
B: superior-temporal			
Intercept	0.1619		
Refraction (D)	0.0286	0.0116	0.021
Optic disc inclination (°)	-0.0284	0.0159	0.09
C: inferior-temporal			
Intercept	0.0589		
Refraction (D)	0.0157	0.0122	0.21
Optic disc size (mm^2)	0.0008	0.1024	0.99
Optic disc inclination (°)	0.0036	0.0165	0.83

Acknowledgements

References

Airaksinen, P.J., Alanko, H.I., 1983. Effect of retinal nerve fibre loss on the optic nerve head configuration in early glaucoma. Graefes Arch. Clin. Exp. Ophthalmol. 220, 193–196.

Airaksinen, P.J., Drance, S.M., Douglas, G.R., Schulzer, M., Wijsman, K., 1985. Visual field and retinal nerve fiber layer comparisons in glaucoma. Arch. Ophthalmol. 103, 205–207.

Airaksinen, P.J., Nieminen, H., Mustonen, H.E., 1982. Retinal nerve fibre layer photography with a wide angle fundus camera. Acta Ophthalmologica 60, 362–368.

Bartling, H., Wanger, P., Martin, L., 2008. Measurement of optic disc parameters on digital fundus photographs: algorithm development and evaluation. Acta Ophthalmologica 86, 837–841.

Denniss, J., McKendrick, A.M., Turpin, A., 2012. The influence of ocular anatomical variables on individual structure-function maps. IVFIS 2012.

Dreher, A.W.R.K., 1992. Retinal laser ellipsometry - A new method for measuring the retinal nerve fiber layer thickness distribution. Clin. Vision Sci., 481–488.

Ferreras, A., Pablo, L.E., Garway-Heath, D.F., Fogagnolo, P., Garcia-Feijoo, J., 2008. Mapping standard automated perimetry to the peripapillary retinal nerve fiber layer in glaucoma. Invest. Ophthalmol. Vis. Sci. 49, 3018–3025.

Fitzgibbon, T., Taylor, S.F., 1996. Retinotopy of the human retinal nerve fibre layer and optic nerve head. J. Comp. Neurol. 375, 238–251.

Garvin, M.K., Abramoff, M.D., Lee, K., Niemeijer, M., Sonka, M., Kwon, Y.H., 2012. 2-D Pattern of Nerve Fiber Bundles in Glaucoma Emerging from Spectral-Domain Optical Coherence Tomography. Invest. Ophthalmol. Vis. Sci. 53, 483–489.

Garway-Heath, D.F., Poinoosawmy, D., Fitzke, F.W., Hitchings, R.A., 2000. Mapping the visual field to the optic disc in normal tension glaucoma eyes. Ophthalmology 107, 1809–1815.

Hee, M.R., Izatt, J.A., Swanson, E.A., Huang, D., Schuman, J.S., Lin, C.P., Puliafito, C.A., Fujimoto, J.G., 1995. Optical coherence tomography of the human retina. Arch. Ophthalmol. 113, 325–332.

Henkind, P., 1967. Radial peripapillary capillaries of the retina. I. Anatomy: human and comparative. Br. J. Ophthalmol. 51, 115–123.

Hoyt, W.F., Frisén, L., Newman, N.M., 1973. Funduscopy of nerve fiber layer defects in glaucoma. Invest. Ophthalmol. Vis. Sci. 12, 814-829.

Iwata, K., Namba, K., Abe, H., 1982. Early fundus changes caused by repeated small crises in the Posner-Schlossman syndrome: a model for glaucoma simplex. Klin. Monbl. Augenheilkd. 180, 20-26.

Jansonius, N.M., Nevalainen, J., Selig, B., Zangwill, L.M., Sample, P.A., Budde, W.M., Jonas, J.B., Lagreze, W.A., Airaksinen, P.J., Vonthein, R., La Levin, Paetzold, J., Schiefer, U., 2009. A mathematical description of nerve fiber bundle trajectories and their variability in the human retina. Vision Res. 49, 2157-2163.

Jeoung, J.W., Kim, T.W., Kang, K.B., Lee, J.J., Park, K.H., Kim, D.M., 2008. Overlapping of retinal nerve fibers in the horizontal plane. Invest. Ophthalmol. Vis. Sci. 49, 1753-1757.

Lamparter, J., Russell R.A., Zhu, H., Asaoka, R., Yamashita, T., Garway-Heath, D.F., 2012. The Importance Of Ocular Anatomical Variables On The Mapping Of Retinal Locations To The Retinal Nerve Fibre Layer And Optic Nerve Head. ARVO 2012.

Lee, K., Kwon, Y.H., Garvin, M.K., Niemeijer, M., Sonka, M., Abramoff, M.D., 2012. Glaucomatous retinal ganglion cell damage is detectable along the entire retinal pathway from macula to optic nerve head using SD-OCT. Arch. Ophthalmol. *In press.*

Mann, I., 1957. Developmental Abnormalities of the eye. British Medical Association, London.

Minckler, D.S., 1980. The organization of nerve fiber bundles in the primate optic nerve head. Arch. Ophthalmol. 98, 1630-1636.

Nouri-Mahdavi, K., Mock, D., Hosseini, H., Bitrian, E., Yu, F., Afifi, A., Coleman, A.L., Caprioli, J., 2012. Pointwise Rates of Visual Field Progression Cluster according to Retinal Nerve Fiber Layer Bundles. Invest. Ophthalmol. Vis. Sci. 53, 2390-2394.

Onwochei, B.C., Simon, J.W., Bateman, J.B., Couture, K.C., Mir, E., 2000. Ocular colobomata. Surv. Ophthalmol. 45, 175-194.

Paetzold, J., Sample, P.A., Selig, B., Krapp, E., Vonthein, R., Schiefer, U., 2005. Differentiation between glaucomatous scotoma progression in depth and in size by using scotoma-oriented perimetry (SCOPE) with locally condensed stimulus arrangements. Invest. Ophthalmol. Vis. Sci. 46, 636.

Quigley, H.A., Enger, C., Katz, J., Sommer, A., Scott, R., Gilbert, D., 1994. Risk factors for the development of glaucomatous visual field loss in ocular hypertension. Arch. Ophthalmol. 112, 644-649.

Radius, R.L., Anderson, D.R., 1979. The course of axons through the retina and optic nerve head. Arch. Ophthalmol. 97, 1154-1158.

Rohrschneider, K., Burk, R.O., Kruse, F.E., Volcker, H.E., 1994. Reproducibility of the optic nerve head topography with a new laser tomographic scanning device. Ophthalmology 101, 1044-1049.

Schiefer, U., Flad, M., Stumpp, F., Malsam, A., Paetzold, J., Vonthein, R., Denk, P.O., Sample, P.A., 2003. Increased detection rate of glaucomatous visual field damage with locally condensed grids: a comparison between fundus-oriented perimetry and conventional visual field examination. Arch. Ophthalmol. 121, 458-465.

Sommer, A., D'Anna, S.A., Kues, H.A., George, T., 1983. High-resolution photography of the retinal nerve fiber layer. Am. J. Ophthalmol. 96, 535–539.

Tanabe, F., Matsumoto, C., Okuyama, S., Takada, S., Hashimoto, S., Arimura, E., Nomoto, H., Kayazawa, T., Eura, M., Shimomura, Y., 2012. Factors in the Retinal Nerve Fiber Layer (RNFL) bundle angles at the optic disc. IVFIS 2012.

Trobe, J.D., 2001. The Neurology of Vision. Oxford University Press, New York, p. 14.

Turpin, A., Sampson, G.P., McKendrick, A.M., 2009. Combining ganglion cell topology and data of patients with glaucoma to determine a structure-function map. Invest. Ophthalmol. Vis. Sci. 50, 3249–3256.

Tuulonen, A., Alanko, H., Hyytinen, P., Veijola, J., Seppanen, T., Airaksinen, P.J., 2000. Digital imaging and microtexture analysis of the nerve fiber layer. J. Glaucoma 9, 5–9.

Vrabec, F., 1966. The temporal raphe of the human retina. Am. J. Ophthalmol. 62, 926–938.

Weber, J., Ulrich, H., 1991. A perimetric nerve fiber bundle map. Int. Ophthalmol. 15, 193–200.

Weinreb, R.N., Dreher, A.W., Coleman, A.L., Quigley, H.A., Shaw, B., Reiter, K., 1990. Histopathologic validation of Fourier-ellipsometry

measurements of retinal nerve fiber layer thickness. Arch.

Ophthalmol. 108, 557-560.

Wigelius, O., 2001. A model for the retinal nerve fiber layer.

Master's thesis in mathematical sciences. Lund University, Sweden.
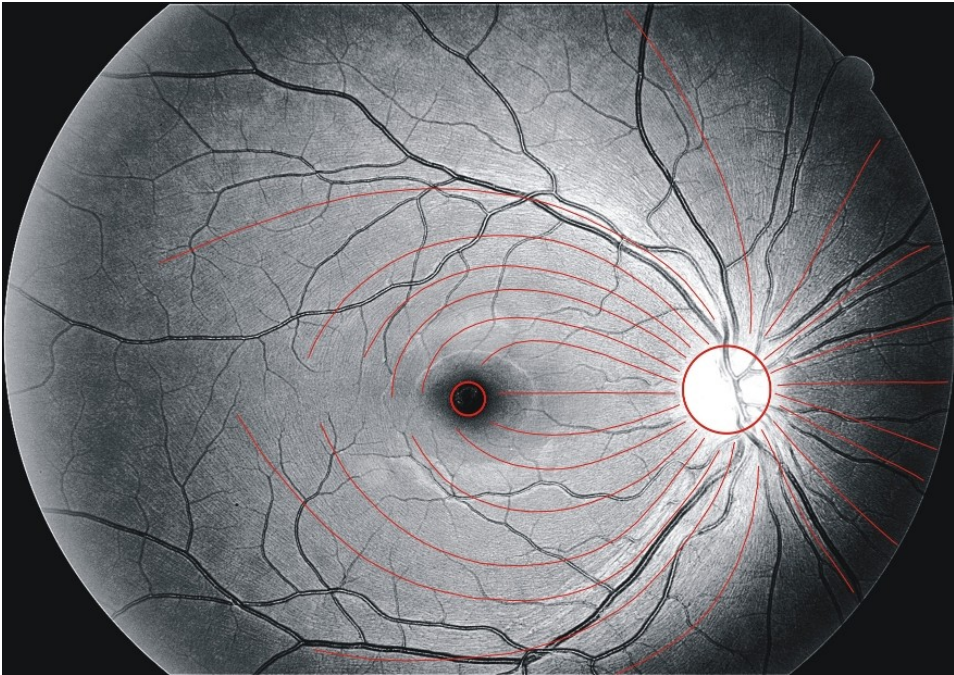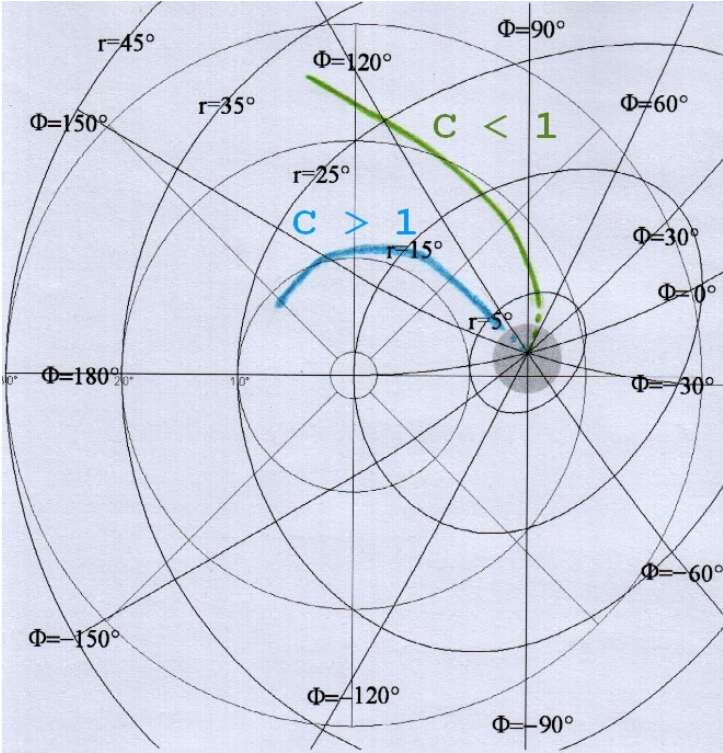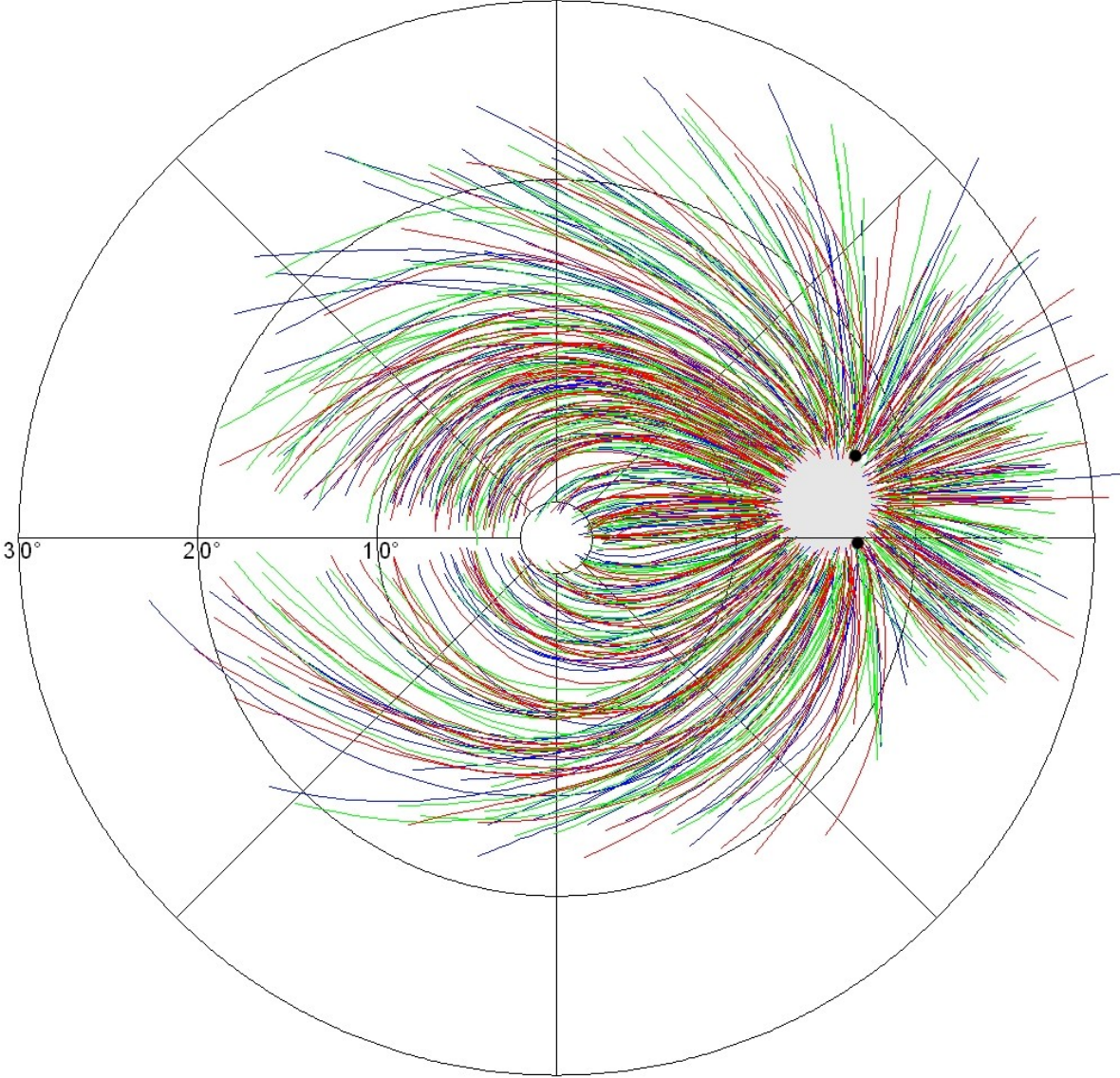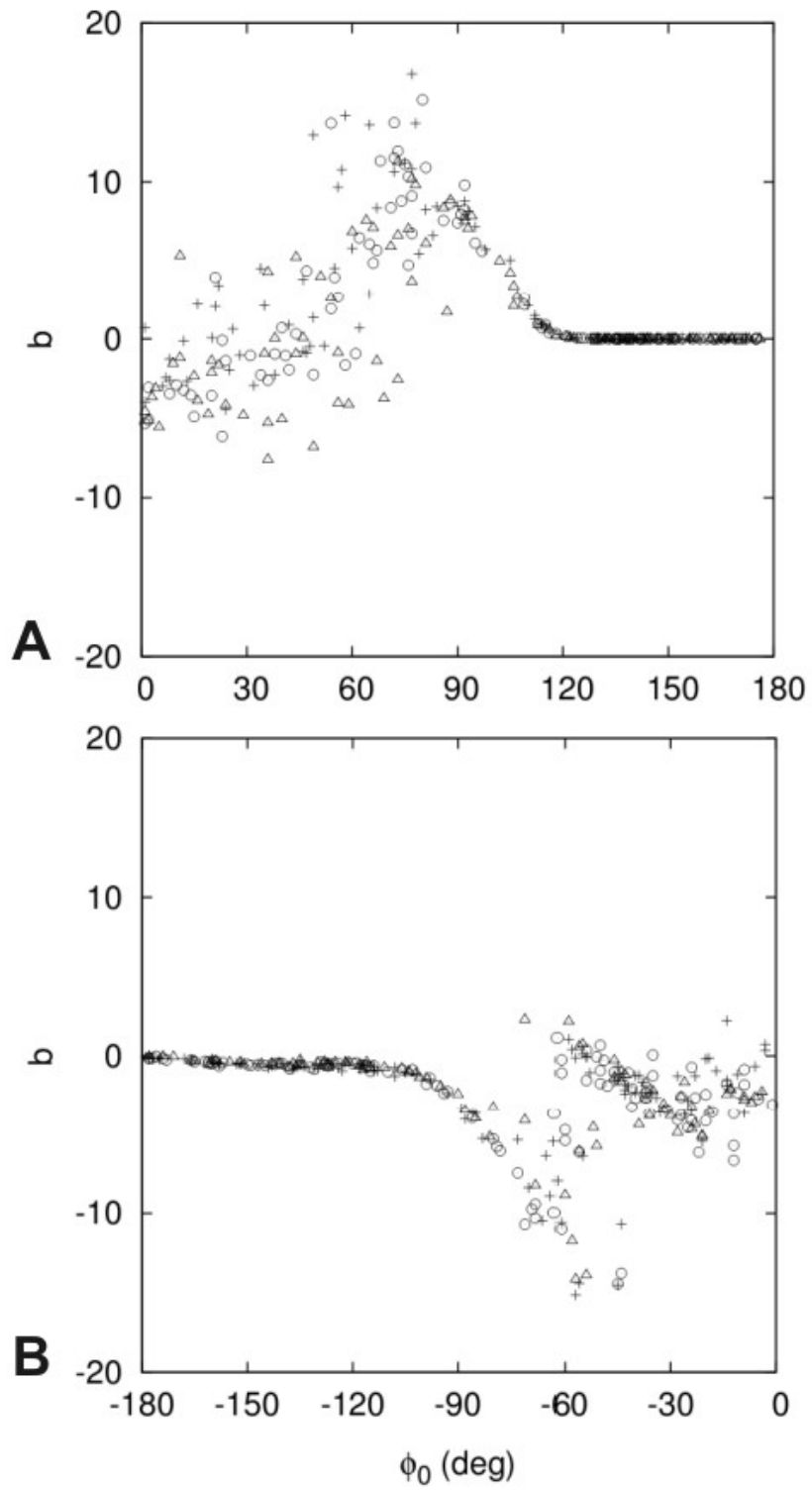
Figure 1

Figure 2

Figure 3

Figure 4

Figure 5

Figure 6

Figure 7

A

B

Figure 8

Figure 9